Engineering Applications of Computational Fluid Mechanics Vol. 8, No. 2, pp. 193–210 (2014)

# PREDICTING FREE-SURFACE VORTICES WITH SINGLE-PHASE SIMULATIONS

Aljaž Škerlavaj*†, Leopold Škerget#, Jure Ravnik# and Andrej Lipej*

*Turboinštitut, Rovšnikova 7, 1210 Ljubljana, Slovenia
#Faculty of Mechanical Engineering, University of Maribor, Smetanova ulica 17,2000 Maribor, Slovenia
† E-Mail: aljaz.skerlavaj@turboinstitut.si (Corresponding Author)

**ABSTRACT:** In this article, single-phase, computational-fluid-dynamics simulations of free-surface vortices are presented. The purpose of the simulations is to determine the appropriate turbulence model for free-surface vortices, which could later be applied to simulations of flow in various engineering systems. The water flow in the laboratory model of a free-surface vortex was numerically simulated by unsteady single-phase computations. The vortex circumferential velocity, the downward velocity inside the vortex core and the predicted length of the free-surface vortex gas core were compared with available measurements. For the two-equation turbulence models, the results indicated the importance of the curvature correction (CC). The effect of the time-step size and the choice of the advection scheme were analyzed. For the tested case, it was determined that the unsteadiness of the flow was insufficient for the correct behavior of the scale-adaptive simulation (SAS) turbulence model. With the CC option, the shear-stress-transport (SST-CC) turbulence model and the SAS-CC turbulence model can both be used for such predictions; however, the SAS-CC model was found to be more reliable. Single-phase simulations successfully predicted the gas-core length for vortices with a short gas core. However, for long cores, the length was under-predicted.

**Keywords:** free-surface vortex, CFD, gas entrainment, pump-intake, turbulence model, curvature correction

## 1. INTRODUCTION

The prediction of free-surface vortices (Fig. 1) is necessary in various engineering systems, most often because of their detrimental effects on the operation of such systems. The presence of vortices in a fluid can cause problems during operations because of the inhomogeneous velocity distribution. An example is the deterioration of the pump's operation due to sub-surface vortices (ANSI/HI, 2012), which can eventually result in pump failure. In addition to an inhomogeneous velocity distribution, free-surface vortices with gas cores can cause gas entrainment from the liquid surface into the engineering systems. In the case of a very strong, downward-velocity gradient, the gas core is extended all the way to the source of the downward velocity in a liquid (Fig. 1, left vortex). It is also possible that bubbles detach from the core tip, or a part of the core is chopped off (Kimura et al., 2008). The bubbles are then entrained into engineering systems because of the strong downward flow in the fluid.

Gas entrainment is particularly undesirable in nuclear reactors where the coolant forms a free-surface, such as in sodium-cooled fast-breeder reactors (SFR) (Sakai et al., 2008). The gas bubbles can cause fluctuations in the reactivity through the void effect, which is inconsistent with the stable operation of the reactor. It is worth mentioning that the gas entrainment in SFRs is not necessarily related only to strong free-surface vortices with a long gas core. Satpathy et al. (2013) made a classification of all the sources of gas entrainment: due to a drain-type vortex (the current study), due to a vortex-induced gas entrainment (Kimura et al., 2008), due to liquid falling on a free surface near the vessel walls (Satpathy et al., 2013), due to shearing at the liquid-gas interface (Durve and Patwardhan, 2012), due to the dissolution of the gas and due to a rotation-induced entrainment near a pump shaft. The vortex-induced gas entrainment occurs in a wake region behind the obstructions due to the high velocity at the fluid surface (Kimura et al., 2008). In this article we deal only with gas entrainment due to a drain-type vortex.

Gas ingestion due to a free-surface vortex can also occur from the tanks or recirculation sumps into the emergency core-cooling system (ECCS), into the decay-heat-removal (DHR) system and/or containment spray (CS) systems after a loss-of-coolant accident (LOCA) in pressurized-water reactors (Blömeling et al., 2010; US NRC, 2006; US NRC, 2008). When referring to the ingestion

*Received: 14 Mar. 2013; Revised: 30 Sep. 2013; Accepted: 25 Nov. 2013*

of gas from recirculation sumps, the case is related to a broader picture of reliable pump operation in pump intakes – it is well known that strong sub-surface or free-surface vortices (the gas entraining being the strongest ones) in pump intakes can have detrimental effects on the pump's operation or even lifetime. The most common examples of pump intakes are the intake for a cooling-water (CW) system of nuclear or thermal power plants, an intake for an essential-service-water (ESW) system of nuclear power plants and intakes for large irrigation systems. In all these systems, strong sub-surface or free-surface vortices are undesirable.

Sakai et al. (2008), who were performing research related to the feasibility of a Japanese SFR (JSFR), proposed design criteria for the prediction of gas entrainment from vortex dimples based on a computational-fluid-dynamics (CFD) method. Such criteria would facilitate the future design of the JSFR. As a part of the research, several cylindrical, free-surface, vortex test vessels (e.g., by Monji et al. (2010)) were designed. The criteria were established based on laminar (i.e., without any turbulence model) single-phase simulations of the vortices in the vessels. The prediction of the length of the gas core of the free-surface vortices was determined in a post-processing phase, based on the assumption of the Burgers vortex model (Burgers, 1948) with respect to the free-surface vortices.

In the reactor vessel of the JSFR (Kimura et al, 2008), as well as in the pump intakes (ANSI/HI, 2012), the flow is turbulent. In order to check the suitability of the turbulence models for the prediction of the free-surface vortices in the JSFR, Ito et al. (2006) designed a free-surface flow case with vortices, shedding from a square rod, and with a suction tube placed below the water surface in the wake region. Two-phase-flow numerical simulations without the turbulence model and with the Renormalization Group (RNG) $k$-ε turbulence model were compared with the experiment. The RNG $k$-ε turbulence model predicted a turbulent viscosity that was too large. This resulted in an underestimated gas entrainment. Although the laminar simulation can predict free-surface vortices well, such a solution will not give a proper prediction of the turbulent bulk flow, which will in turn affect the prediction of the vortices (their position and strength). Therefore, it is worth finding a suitable turbulence model for such flows. It should be mentioned that Merzari et al. (2009) tested large-eddy simulation (LES) and detached-eddy simulation (DES) turbulence models on a case of a free-surface vortex model and obtained slightly better results with the LES model.

The current study presents a thorough test of the behavior of turbulence models on a Monji's vortex case (Monji et al., 2010), which was a reference case for the study of Sakai et al. (2008). Like in the latter study, the simulations were performed as single-phase simulations, and the previously mentioned method of prediction for the length of the gas core of the free-surface vortices was used in a post-processing phase. Although it would be natural to think first of a two-phase (water and air) simulation for accurate predictions of the vortices in the pump sump, such a simulation demands a lot of computing power. In general, two-phase flow simulations need a very fine mesh to resolve the gas-liquid interface accurately. This is the case for the homogeneous and the inhomogeneous type of two-phase model. In cases such as the JSFR vessel or a pump intake, free-surface vortices often appear intermittently and change their location, which means that the simulations should be performed as transient ones and that it is important to make a fine mesh for the whole region in which the vortices with gas cores may appear. Ito et al. (2009) developed a high-precision volume-of-fluid algorithm for numerical simulations of gas-entrainment phenomena. The validation was performed for a vortex with a fully developed gas core that reached the suction mouth. Blömeling et al. (2010) have tried to use a homogeneous, Eulerian-Eulerian, two-phase model and obtained an underestimated length for the gas core. On the other hand, Merzari et al. (2009) performed simulations of a free-surface vortex with single-phase and homogeneous two-phase models. The single phase model incorrectly predicted peak downward velocity near the water surface. The two-phase model correctly predicted the shape of a vortex gas core of a fine mesh, whereas the length of the gas core was underestimated for a slightly coarser mesh.

Because single-phase simulations need less computing power than two-phase simulations, it is desirable to perform a single-phase (water) simulation instead. In such a case the information about the gas core of the vortex, which might start to entrain air into the pump bell, is lost. An additional vortex model is needed to convert a single-phase result into a result with a physical meaning. For instance, the vortex may be treated as a Rankine vortex (as was the case with Li et al. (2008)) for its simplicity, or a Burgers vortex (Burgers, 1948) (as was the case with Sakai et al. (2008) and by Okamura and Kamemoto (2005))

for its ability to predict the axially accelerated vortices.

Fig. 1 Free-surface vortices (type VI from the classification in ANSI/HI; 2012) appearing in badly designed pump-intake structure. White arrow: flow direction; solid line: sharp wall corners; dashed line: water surface level; black arrows and dotted lines: indication of surface vortices and length of their gas cores, respectively. Source: photo archive of Turboinštitut (Pumps Programme).

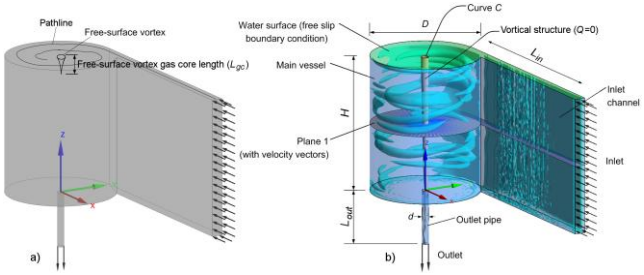


Fig. 2 Test-case geometry: (a) scheme of free-surface vortex appearing in laboratory model; (b) typical vortical structures of numerical model (iso-surface $Q$=0 s$^{-2}$).

For the test case, the outlet-pipe Reynolds number varied between 5,900 and 10,500, depending on the discharge rate setting. In other engineering cases, often a higher (but sometimes also a lower) Reynolds number may be needed. For instance, in experimental tests of the suitability of pump-intake models (Fig. 1), where the strength of the sub-surface and free-surface vortices is observed, the Reynolds number at the pump's bell mouth exceeds 60,000 (ANSI/HI, 2012). By using such a high value a similarity of the flow between the pump-intake model and the prototype is assured, because the scaling of structures with a free-surface (as opposed to closed conduit systems) is performed for the Froude number (and not the Reynolds number) similarity. Despite the somewhat lower Reynolds number in the observed case, the flow behavior and the conclusions are in accordance with our similar studies for a higher Reynolds number. The first such study (Škerlavaj et al., 2011) was of subsurface vortices (for a pump bell Reynolds number of 1.7 x $10^5$). There it was concluded that the scale-adaptive simulation turbulence model with the curvature correction (SAS-CC) was an optimal turbulence model, and that even a shear-stress transport model with a curvature correction (SST-CC) might be a possible choice for the bottom part of the floor vortex. The Reynolds stress models (RSMs) were computationally too expensive, whereas the result of the baseline explicit algebraic RSM model (BSL EARSM) was (in addition to the long computational time needed) not any better than that of the SST model. The second study, partially presented in (Škerlavaj, 2011), was a successful test of the procedure described in this article for the simulation of a pump-intake model (for a Reynolds number of 6.0 x $10^4$) with two free-surface vortices, using the SAS-CC turbulence model. The goal of the present article is, therefore, to determine which (if any) of the turbulence models might be suitable for the simulations of free-surface vortices for flows in various engineering systems, for instance in some nuclear-reactor vessels or in pump intakes.
The CFD simulations were performed by the commercial CFD solver Ansys CFX (2011), which uses an element-based finite-volume method.

## 2. TEST-CASE MODEL

The test-case geometry (Fig. 2) is based on one of the physical models used for measurements by Monji et al. (2010). The diameter $D$ of the cylindrical vessel (Fig. 2) is 0.2 m, the width of the inlet channel is 0.02 m, and the diameter $d$ of the outlet pipe is 12.5 mm. The vessel was filled with water up to the level $H$=0.25 m from the bottom of the vessel. In the simulations the length of the shorter side of the inlet channel ($L_{in}$) was 0.34 m and the outlet pipe length ($L_{out}$) was 0.1 m. The water flows into a narrow open channel and then enters into the cylindrical vessel at its side. The water rotates in the vessel (Fig. 2a) and exits through the outlet pipe at the bottom of the vessel. Due to the rotation a free-surface vortex is formed in the centre of the vessel. The water surface at the vortex core is deformed and such an air core can be a few centimeters long ($L_{gc}$). In the experiment, the relationship between the inlet discharge rate $Q$ and the length of the vortex gas

core $L_{gc}$ was observed, up to the start of the air-bubble detachment from the tip of the free-surface vortex gas core. The values of the dimensionless numbers and their definitions are presented in Table 1.

The vortex test model in the study of Monji et al. (2010) was designed to represent a free-surface vortex in a reactor vessel of JSFR. This test case can also be used for a study of the free-surface vortex occurring in a pump sump, as the liquid level is similar to the liquid level inside the model of the pump intake and the average velocity inside the outlet pipe is similar to the average velocity at the pump bell entrance of the model of the pump intake. For instance, in one of our commercial projects involving pump-intake model testing, the liquid level was 0.305 m and the average velocity at the pump bell entrance was 0.91 m/s. For the observed case of the study of Monji et al. (2010), the liquid level was 0.25 m and the average velocity in the outlet pipe was between 0.61 m/s and 1.06 m/s, depending on the discharge rate observed.

Table 1 Non-dimensional numbers. The $\mathrm{Re}_{vortex}$ was assessed from the laminar simulations. The Froude numbers are calculated as $\mathrm{Fr}_d = U/\sqrt{g \cdot d}$ and $\mathrm{Fr}_H = U/\sqrt{g \cdot H}$. Weber number is calculated as $\mathrm{We} = \rho U^2 d/\sigma$.

| Discharge rate [l/min] | $\mathrm{Re}_d$ | $\mathrm{Re}_{vortex}$ | We | $\mathrm{Fr}_d$ | $\mathrm{Fr}_H$ |
|---|---|---|---|---|---|
| 4.5 | 7,600 | 6,800 | 64 | 1.75 | 0.390 |
| 5 | 8,400 | 7,800 | 79 | 1.94 | 0.434 |
| 6 | 10,100 | 9,900 | 114 | 2.33 | 0.520 |
| 7 | 11,800 | 12,200 | 155 | 2.71 | 0.607 |
| 7.5 | 12,700 | 13,500 | 178 | 2.91 | 0.650 |
| 7.8 | 13,200 | 14,100 | 193 | 3.03 | 0.676 |

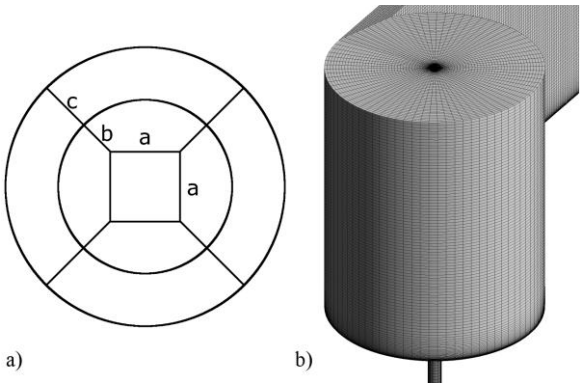


Fig. 3 Test-case computational mesh: (a) mesh topology sketch; (b) mesh.

## 3. NUMERICAL MODEL

### 3.1 Computational mesh

A block-structured mesh with 790,000 elements was used (Fig. 3). The number of elements on the vessel surface is 20 per edge "a" (Fig. 3a), 15 per edge "b" and 43 per edge "c". The number of nodes in the *Z*-direction inside the main vessel is 110. The height of the first element at the water surface and of the elements inside the vessel (in *Z*-direction) is 3 mm. In the radial direction, the height of the first element at the vessel wall (edge "c") is 2.5 mm. The minimum orthogonality angle was 26.5, the maximum expansion factor was 3 and the maximum aspect ratio was 84. The calculated average $y^+$ values with the SAS-CC turbulence model were below 2.5 at the vessel bottom and up to 7.5 at the vessel walls for the 6 l/min discharge case.

The type of the problem was found to be prohibitive for a mesh independence study with the Courant number equal to one and with the number of elements being multiplied by a factor of two in each direction. The main reason was the long simulation time (1150 s). The secondary reason is that denser meshes need smaller time-step sizes to yield the same Courant number as the sparser ones. As the CFX is an implicit solver and therefore the solution is stable even for Courant numbers larger than one, the simulations with the SAS-CC model were performed on two other meshes (at discharge rate 6 l/min), the one with 4.2 million and the other one with 17.3 million elements, with the same time-step size (0.01 s). Both results were qualitatively similar to that obtained with the mesh presented in this article – the predicted circumferential velocity in the potential (outer) part of the vortex was closer to the measured values, but it was still higher than the measured values (Škerlavaj, 2011).

### 3.2 Boundary conditions

The test case was calculated as a single-phase simulation with a flat water surface, specifying a free-slip boundary condition at the water surface. A flat water surface is a common practice in single-phase simulations of pump-intake models, used for instance by Rajendran et al. (1999), Ito et al. (2010) and Matsui et al. (2006). For the walls, a no-slip boundary condition was specified. For the inlet boundary condition (Fig. 2) the mass flow was specified according to the data in Monji et al. (2010) and for the outlet an average static pressure was specified. It was tested to ensure that

the inlet channel was long enough for the laminar profile to develop. In cases where turbulence models were used, a one-percent turbulence intensity was specified at the inlet. A separate simulation of a channel flow revealed that the velocity profile obtained with one percent of turbulence intensity was similar to the one obtained with a laminar simulation. For the plane $Z$=0.125 m, the maximum velocity for the SST model was two percent smaller than the one predicted with the laminar simulation. In addition, based on a comparison of the velocity field between a five-percent and a one-percent inlet turbulence intensity in a vortex model vessel, it was concluded that the impact of the inlet turbulence intensity on the result could be neglected.

The number of simulations needed for the comparisons was large, as the measurements of the downward velocity, the circumferential velocity and the length of the free-surface vortex gas core in the work of Monji et al. (2010) were performed for different volumetric flow rates. Namely, at 20 ℃ the circumferential velocity was measured at 4.5 l/min and 6 l/min, the downward velocity was measured at 4.5 l/min and 7.8 l/min and the length of the free-surface vortex gas core was measured at 5, 6, 7 and 7.5 l/min. Forty-two of the simulations that were performed are presented in Table 2.

### 3.3 Numerical schemes

Several types of advection schemes were tested in the simulations. The advection schemes can be written in the form $\varphi_{ip} = \varphi_{up} + \beta \cdot \partial\varphi/\partial x_j \cdot \left(x_{ip} - x_{up}\right)_j$, where $\varphi_{ip}$ represents the value of a scalar variable at the integration point $ip$, $\varphi_{up}$ is the value at the upwind node and $(x_{ip}\text{-}x_{up})_j$ is a component of a vector from the upwind node to the integration point (ANSYS, 2011). The subscript $j$ represents the Einstein summation notation. A particular choice of the correction factor β and $\partial\varphi/\partial x_j$ yields different schemes that were used in the simulations (Table 2).

For the scheme that was denoted a ‘second-order’ scheme in Table 2, the β was set to one and $\partial\varphi/\partial x_j$ was set to the average of the adjacent nodal gradients (ANSYS, 2011). The gradients at the nodes (of a general scalar variable φ) are computed using Gauss’ divergence theorem as

$$\partial\varphi/\partial x_j = \frac{1}{V}\sum_{ip}\left(\varphi\, n_j\right)_{ip} \tag{1}$$

where $n_j$ is a component of the outward-pointing normal vector of the surface segment through an integration point and $V$ is the volume around the node. The scheme is formally second-order accurate in space, but it is unbounded and may produce non-physical oscillations.

Table 2 Computation matrix.

| Turb. model | Num. scheme | Time-step | Discharge rate [l/min] |
|---|---|---|---|
| Laminar | high-resolution | 0.1 s | 4.5, 6, 7 and 7.8 |
| Laminar | high-resolution | 0.001 s | 6 |
| Laminar | Second order | 0.1 s | 4.5, 5, 6, 7, 7.5 and 7.8 |
| Laminar | Second order | 0.01 s | 6 |
| Laminar | Second order | 0.001 s | 6 |
| $k$-ε RNG | high-resolution | 0.1 s | 4.5 |
| SST | high-resolution | 0.1 s | 4.5 |
| SST-CC | high-resolution | 0.1 s | 4.5, 6, 7 and 7.8 |
| SST-CC | high-resolution | 0.01 s | 4.5, 6, 7 and 7.8 |
| SAS | high-resolution | 0.01 s | 4.5, 6 and 7.8 |
| SAS-CC | high-resolution | 0.1 s | 4.5 |
| SAS-CC | high-resolution | 0.01 s | 4.5, 6, 7 and 7.8 |
| SAS-CC | Second order | 0.01 s | 4.5, 5, 6, 7, 7.5 and 7.8 |
| SAS-CC | Hybrid | 0.01 s | 6 |
| SAS-CC | high-resolution | 0.001 s | 4.5, 6, 7 and 7.8 |

The second scheme that was used, and which is also the default scheme for the SST model in the Ansys CFX solver, was the 'high-resolution' (HR) scheme (ANSYS, 2011). The scheme is a bounded, second - order, upwind - biased discretization, which limits the numerical advection correction (the term $\beta \cdot \partial\varphi/\partial x_j \cdot \left(x_{ip} - x_{up}\right)_j$) in order to suppress possible oscillations due to large gradients. In this scheme, the values of β and $\partial\varphi/\partial x_j$ from the upwind node are used. The value of β is calculated using the methodology of Barth and Jespersen (1989). First, the bounding values $\varphi_{min}$ and $\varphi_{max}$ are determined for each node. Then, for each integration point, the value of $\beta_{ip}$ is limited to ensure that $\varphi_{min} \le \varphi_{ip} \le \varphi_{max}$. The nodal value of β is the minimum value of all the $\beta_{ip}$ surrounding the node. The value of β is also limited by 1. When this scheme was used in the simulations, no label about the scheme is given in the graphs.

The third scheme used was the hybrid scheme (Strelets, 2001). The scheme is a blending between the central-difference scheme (CDS) in the LES regions and the high-resolution scheme in the RANS regions. The blending is achieved with the blending function σ as $\varphi_{ip} = \sigma\varphi_{ip,U} + (1-\sigma)\varphi_{ip,C}$, where the subscripts *U* and *C* represent the upwind and central-difference schemes, respectively. The blending function σ is a function of $C_{DES}\Delta_{max}/L$, where *L* is a turbulent length scale, $\Delta_{max}$ is the maximum length of a neighboring grid edge and $C_{DES}$ is a value, blended between 0.61 and 0.78 in the *k*-ε and *k*-ω region, respectively. The value of σ is close to zero in the LES regions and close to one in the RANS regions. In addition, in irrotational regions the upwind scheme is used.

The second-order backward Euler transient scheme was used as an implicit time-stepping scheme. The scheme is not bounded.

### 3.4 Time-averaging method

All the cases were calculated as transient runs. The convergence criterion for each time step was set to $10^{-5}$ for the RMS velocity residuals. If the magnitude was not satisfied within 10 loops per time step, the simulation would proceed with the next time step. The total simulation time was 1150 s. The vortex core is fully formed after 600 s, which was determined in analyses of each simulation result by observing the instantaneous values of downward velocity, the vortex gas-core length and the maximum circulation.

The simulation results were compared to measurement data published in the work of Monji et al. (2010). The comparison was made for the time-average circumferential velocity, the highest downward velocity inside the core of the vortex (colored-dye velocity in the experiment; from now on denoted as 'downward velocity'), and for the vortex gas-core length. The comparison was made at a water temperature of 20 ℃.

Statistical averaging was performed from 600 s onwards. The average circumferential velocity was obtained from the averaged velocity field. The downward velocity and the vortex gas-core length were, however, averaged over the instantaneous values written to the transient files at 5 s intervals from time 600 s onwards. The instant downward velocities were calculated as the maximum downward velocity near the vortex core, determined for *Z*-planes with a *Z*-step size of 0.001 m.

To estimate the statistical error ε of the mean values of the downward velocity and of the vortex gas-core length a procedure by Mockett et al. (2010) was used. In general, the difficulty in estimating the error is that the true mean value of an observed variable $\bar{\varphi}$ cannot be known because the statistical sample is always of a finite length. One way of estimating the statistical error is to divide a signal of length *T* into a series of windows of length $T_w$. Such a statistical error depends on the window size and is estimated as

$$\varepsilon(T_w) \approx \sqrt{\left\langle (\hat{\varphi}_{Tw} - \hat{\varphi}_T)^2 \right\rangle} / \hat{\varphi}_{Tw} \qquad (2)$$

where $\hat{\varphi}_T$ is the mean value of a variable in a signal of length *T*, $\hat{\varphi}_{Tw}$ is the mean value in the observed window $T_w$ and the symbol $\langle\ \rangle$ is used for averaging over the windows (Mockett et al., 2010). When $T_w$ approaches *T* the estimation becomes unreliable because of the small number of windows available. Mockett et al. (2010) have provided a procedure to estimate the error conservatively. The error for the mean value is based on an analytical expression for a bandwidth-limited Gaussian white noise and is estimated as

$$\varepsilon \approx \frac{1}{\sqrt{2BT}} \left( \frac{\sigma_T}{\hat{\varphi}_T} \right) \qquad (3)$$

where $\sigma_T$ is the standard deviation of a signal of size *T*. The unknown parameter *B* is determined by fitting the curve from Eq. (2). Mockett et al. (2010) have shown that for all the values of $T_w$ the error from Eq. (3) is larger than or equal to the

error from Eq. (2), and that even for large $T_w$ the error can still be quantified.

The final simulation time of 1150 s was long enough to apply the procedure by Mockett et al. (2010), because in most cases a window size (of the moving average) of approximately five values (corresponding to 25 s) was sufficient to satisfy the necessary condition $BT \geq 5$. A longer final time of the simulations (1150 s) resulted in smaller values of the error of the mean values. In the case of the downward velocity, the error ε was estimated to be smaller than 1.5% for laminar simulations, smaller than 1% for SAS-CC simulations and smaller than 0.7% for SST-CC simulations. In the case of the vortex gas-core length, the error of the laminar, SAS-CC and SST-CC values was estimated to be smaller than 7.5%, 3.7% and 3.9%, respectively. It should be mentioned that the 95% confidence interval for the true mean value $\overline{\varphi}$ (for infinite sample length) is given by $\hat{\varphi}_T/(1+2\varepsilon) \leq \overline{\varphi} \leq \hat{\varphi}_T/(1-2\varepsilon)$ (Mockett et al., 2010).

## 4. TURBULENCE MODELS

The purpose of the present study is to find a suitable turbulence model for (single-phase) simulations of the free-surface vortices in some engineering systems. Traditionally, for free-surface vortices the inviscid (Ansar et al. 2002) or laminar (Sakai et al. 2008) simulations were often used, as they can predict the vortex filaments stretching and the diffusion of the vorticity is not too large. In contrast, because of the locally large eddy viscosity the standard RANS models tend to predict only very large-scale vortical structures, either in the case of vortical or unstable flow. As pointed out by Menter et al. (2010), such behavior is not a result of the averaging procedure itself, but from the conception of the RANS models. With a proper formulation of RANS models (either by the inclusion of the von Karman length scale in its transport equations or by the inclusion of the 'curvature-correction' option), the improved models can predict results that are as accurate as the Reynolds stress models, as shown, for instance, in Shur et al. (2000). With the recent progress in turbulence modeling, the newly formulated two-equation RANS models might be appropriate for the prediction of free-surface vortices, which would place them in a superior position to inviscid or laminar simulations, as the flow in many engineering systems (e.g., pump intakes) is turbulent.

Besides laminar simulations (i.e., without any turbulence model), simulations with several turbulence models were performed in the current study: RNG *k*-ε, SST, SST-SAS and Zonal LES in combination with SST-SAS. The SST and SST-SAS turbulence models were calculated with and without the curvature correction (CC). The laminar simulation was performed because of the viscous core of the main vortex (Fig. 2) and as a result of the positive results in the study of Sakai et al. (2008). The RSM and EARSM models were not tested because of the long computing times (Škerlavaj et al., 2011).

### 4.1 Two-equation RANS models

The standard, two-equation turbulence models are well known. The models in this group have two additional transport equations in order to represent the turbulent properties of the flow.

The RNG *k*-ε model (Yakhot et al., 1992) is based on the renormalization group analysis of the Navier–Stokes equations. It has the same transport equations for the turbulence kinetic energy *k* and for the dissipation rate of the turbulence kinetic energy ε as the standard *k*-ε model, but has slightly different model constants. The constant $C_{\varepsilon 1}$ (which is multiplied by the production term $P_k$ in the ε transport equation) is replaced by the function (ANSYS, 2011)

$$C_{\varepsilon 1\mathrm{RNG}} = 1.42 - \frac{\eta\left(1-\frac{\eta}{4.38}\right)}{1+\beta_{\mathrm{RNG}}\eta^3};\ \eta = \sqrt{\frac{P_k}{\rho C_{\mu\mathrm{RNG}}\varepsilon}} \quad (4)$$

where ρ is the fluid density, ε is the turbulence dissipation rate, whereas $\beta_{\mathrm{RNG}}$ and $C_\mu$ are constants equal to 0.012 and 0.085, respectively. Occasionally, (e.g., see Galván et al. (2011)) the RNG *k*-ε model is reported to produce better results for swirling flows than the standard *k*-ε model. It should be noted, however, that the RNG model in Fluent code includes a swirl modification for the eddy viscosity, which might be the main reason for the good results of the RNG model in the case of Galván et al. (2011).

The SST turbulence model is a very frequently used model. It is a blend between the *k*-ε model, used in the domain interior, and the *k*-ω model, used near walls. It also limits the eddy viscosity. The version of the SST turbulence model used in the study was presented by Menter et al. (2003). The *k* and ω equations read as

$$\frac{\partial(\rho k)}{\partial t} + \frac{\partial}{\partial x_j}\left(\rho \bar{u}_j k\right) = \tilde{P}_k - \beta^* \rho k\omega + \frac{\partial}{\partial x_j}\left[\left(\mu + \sigma_{k3}\mu_t\right)\frac{\partial k}{\partial x_j}\right] \quad (5)$$

$$\frac{\partial(\rho\omega)}{\partial t}+\frac{\partial}{\partial x_j}\left(\rho\bar{u}_j\omega\right)=\alpha_3\frac{\omega}{k}\tilde{P}_k-\beta_3\rho\omega^2 + 2(1-F_1)\rho\sigma_{\omega 2}\frac{1}{\omega}\frac{\partial k}{\partial x_j}\frac{\partial\omega}{\partial x_j}+\frac{\partial}{\partial x_j}\left[\left(\mu+\sigma_{\omega 3}\mu_t\right)\frac{\partial\omega}{\partial x_j}\right] \quad (6)$$

where the constant $\beta^*$ is equal to 0.09, $\rho$ is the fluid density, $\bar{u}_j$ is a component of the average velocity, $\mu$ is the dynamic viscosity, $k$ is the turbulence kinetic energy and $\omega$ is the turbulence eddy frequency. The Einstein summation convention is used. The constants with the index 3 are linear combinations that result from the blending of the underlying $k$-$\varepsilon$ and $k$-$\omega$ models and are calculated as $\Phi_3=F_1\Phi_1+(1-F_1)\Phi_2$, where $\Phi$ represents a respective constant and the indices 1 and 2 represent the values from the $k$-$\omega$ and transformed $k$-$\varepsilon$ equations, respectively. The blending function $F_1$ is defined by

$$F_1=\tanh\left(\left(\min\left[\max\left(\frac{\sqrt{k}}{\beta^*\omega y},\frac{500\mu}{y^2\omega\rho}\right),\frac{4\rho\sigma_{\omega 2}k}{CD_{k\omega}y^2}\right]\right)^4\right) \quad (7)$$

where $y$ is the distance to the nearest wall and

$$CD_{k\omega}=\max\left(2\rho\sigma_{\omega 2}\frac{1}{\omega}\frac{\partial k}{\partial x_j}\frac{\partial\omega}{\partial x_j},10^{-10}\right) \quad (8)$$

The eddy viscosity is defined by

$$\mu_t=\frac{a_1 k\rho}{\max(a_1\omega,F_2 S)}. \quad (9)$$

The magnitude of the strain rate is defined by

$$S=(2S_{ij}S_{ij})^{1/2};\ S_{ij}=\frac{1}{2}\left(\frac{\partial\bar{u}_i}{\partial x_j}+\frac{\partial\bar{u}_j}{\partial x_i}\right) \quad (10)$$

The second blending function $F_2$ is defined by

$$F_2=\tanh\left(\left[\max\left(\frac{2\sqrt{k}}{\beta^*\omega y},\frac{500\mu}{y^2\omega\rho}\right)\right]^2\right) \quad (11)$$

The production term is defined by

$$\tilde{P}_k=\min\left(\mu_t\frac{\partial\bar{u}_i}{\partial x_j}\left(\frac{\partial\bar{u}_i}{\partial x_j}+\frac{\partial\bar{u}_j}{\partial x_i}\right),10\cdot\beta^*\rho k\omega\right) \quad (12)$$

Finally, the constants are given as: $\alpha_1$=5/9, $\beta_1$=3/40, $\sigma_{k1}$= 0.85, $\sigma_{\omega 1}$= 0.5, $\alpha_2$=0.44, $\beta_2$=0.0828, $\sigma_{k2}$=1, $\sigma_{\omega 2}$= 0.856 and $a_1$=0.31.

### 4.2 SAS model

The SAS turbulence model is a recent development. The version of the model used in this study is thoroughly described in the work of Egorov and Menter (2008). The model was developed as the $k$-$\sqrt{k}L$ model, where $L$ is an integral length scale of the turbulence, and then transformed into the SST-SAS model. The SST-SAS model is an SST model with an additional source term $Q_{SAS}$ in the $\omega$ transport equation (Egorov and Menter, 2008),

$$Q_{SAS}=\max\left[\rho\zeta_2\kappa S^2\left(\frac{L}{L_{vK}}\right)^2 - C_{SAS}\frac{2\rho k}{\sigma_\Phi}\max\left(\frac{1}{\omega^2}\frac{\partial\omega}{\partial x_j}\frac{\partial\omega}{\partial x_j},\frac{1}{k^2}\frac{\partial k}{\partial x_j}\frac{\partial k}{\partial x_j}\right),0\right] \quad (13)$$

with

$$L_{vK}=\kappa\left|\frac{U'}{U''}\right|;\ L=\sqrt{k}/\left(c_\mu^{1/4}\omega\right);\ U''=\sqrt{\frac{\partial^2\bar{u}_i}{\partial x_k^2}\frac{\partial^2\bar{u}_i}{\partial x_j^2}};\ U'=\sqrt{2S_{ij}S_{ij}} \quad (14)$$

where $S_{ij}$ represents the components of the strain rate tensor, $u_i$ is a component of the velocity vector, and the values of the constants are $\zeta_2=3.51$, $\sigma_\Phi=2/3$, $C_{SAS}$=2, $\kappa=0.41$ and $c_\mu=0.09$. The main difference between the SST-SAS and the standard RANS two-equation models is that the SAS model includes the von Karman length scale $L_{vK}$ in the $\omega$ transport equation. In unsteady zones the $L_{vK}$ is decreased, which increases the $Q_{SAS}$, which in turn increases $\omega$ and subsequently decreases the eddy viscosity $\mu_t$. As a result, the SAS model can develop LES-like solutions in the unsteady zones. In the event that the LES-like solution cannot be resolved properly, for instance, due to a time-step size that is too large, the model adjusts the eddy viscosity and will eventually revert to a RANS solution, as presented by Menter and Egorov (2010).

### 4.3 Curvature correction

One of the well-known weaknesses of the conventional one- and two-equation RANS models is their inability to capture the effects of the streamline curvature and the system rotation (Bradshaw, 1973; Patel and Sotiropoulos, 1997; Leschziner and Drikakis, 2002; York et al., 2009). For these RANS models the eddy viscosity scalar replaces the Reynolds stress tensor to close the system of equations. The models cannot predict the curvature and rotation effects because of the isotropic nature of the eddy-viscosity concept. In order to sensitize the models to the curvature and rotation effects, many variants of the corrections of the turbulence models exist (e.g., by Launder et al., 1977; Pettersson Reif et al., 1999; Spalart and Shur, 1997; Cazalbou et al., 2005).

The curvature-correction (CC) function that is used in this paper was first presented in the work of Spalart and Shur (1997) in conjunction with the Spalart-Allmaras (SA) turbulence model. The main idea of the function is to track the rate of change of the principal axes of the strain tensor. The function is Galilean invariant and unifies the

rotation and curvature effects. The corrected form for the CC in conjunction with the SA model was given in Shur et al. (2000). The form used in this paper was presented by Smirnov and Menter (2009) as

$$f_{\text{rotation}} = (1+c_{\text{r1}})\frac{2r^*}{1+r^*}\left[1-c_{\text{r3}}\tan^{-1}\left(c_{\text{r2}}\tilde{r}\right)\right]-c_{\text{r1}} \quad (15)$$

The non-dimensional quantities $r^*$ and $\tilde{r}$ were defined by

$$r^* = \frac{S}{\Omega};\ \tilde{r} = 2\Omega_{ik}S_{jk}\left[\frac{\mathrm{D}S_{ij}}{\mathrm{D}t}+\epsilon_{imn}S_{jn}+\epsilon_{jmn}S_{in}\right)\Omega_m^{rot}\Bigg]\frac{1}{\Omega D^3} \quad (16)$$

where $\Omega_m^{rot}$ are components of the vorticity vector of a reference frame and $\mathrm{D}S_{ij}/\mathrm{D}t$ are the components of a Lagrangian derivative of the strain tensor. The Einstein summation convention is used and $\epsilon_{ijk}$ is a Levi-Civita symbol. The magnitude of the strain rate $S$ is defined by Eq. (10), whereas the magnitude of the vorticity rate $\Omega$ is defined by the vorticity tensor as $\Omega = (2\Omega_{ij}\Omega_{ij})^{1/2}$, where

$$\Omega_{ij} = \frac{1}{2}\left(\left(\frac{\partial\overline{u}_i}{\partial x_j}-\frac{\partial\overline{u}_j}{\partial x_i}\right)+2\epsilon_{\text{mji}}\,\Omega_m^{rot}\right) \quad (17)$$

The value of $D$ was defined by $D^2 = \max\left(S^2, 0.09\omega^2\right)$ and the empirical constants were set to $c_{r1}$=1.0, $c_{r2}$=2.0 and $c_{r3}$=1.0.

The curvature-correction option, in conjunction with the SST or SAS model, multiplies the production term in the $k$ and ω transport equations by the upwards- and downwards-limited, CC function $f_{\text{rotation}}$ (Smirnov and Menter, 2009; ANSYS, 2011).

Spalart and Shur (1997) have shown that it is not easy to anticipate the correlations between the flow streamlines, the values of curvature correction function and the eddy viscosity. According to Smirnov and Menter (2009), the correction only adds approximately one percent of the CPU time per iteration. It should be noted that with the inclusion of the CC option the convergence rate can be degraded and thus more iterations per time step might be needed (Škerlavaj et al., 2011). Smirnov and Menter (2009) and Shur et al. (2000) have thoroughly tested the CC function in conjunction with the SST and the SA turbulence models and have reported that for many types of flow the results can be as good as the ones with the Reynolds-stress turbulence models.

## 5. METHOD OF GAS-CORE LENGTH DETERMINATION

The method is based on that described in the study of Sakai et al. (2008), with some modifications. The basic equation for the gas-core length prediction does not include the water's surface tension and is determined by

$$L_{gc} = \frac{\ln 2\cdot\alpha\Gamma_\infty^2}{4g\nu(2\pi)^2} \quad (18)$$

where α is the downward-velocity gradient in the Burgers (1948) vortex model, $\Gamma_\infty$ is the circulation of the vortex, ν is the kinematic viscosity and g represents the acceleration due to gravity. The equation was derived in the study of Ito et al. (2010) based on the Burgers (1948) vortex model. It should be noted that due to typographical errors the correct equation is given in Sakai et al. (2008).

The first modification is in the method for selecting the vortex centre. Partially due to the influence of the mesh and the strong gradients, and partially due to the definition of the vortex itself, it was decided to define a pivot point at the water surface as the centroid of the water surface, bounded by the value of the invariant $Q$ = 0 $s^{-2}$ (the central point in Fig. 4). The $Q$ criterion (Hunt et al., 1988) is a method for determining vortical structures in incompressible flows, defined by

$$Q = \frac{1}{2}\left(\Omega_{ij}\Omega_{ij}-S_{ij}S_{ij}\right) = \frac{1}{4}\left(\Omega-S\right) > 0 \quad (19)$$

where Ω is the magnitude of the vorticity rate and S is the magnitude of the strain rate. The $\Omega_{ij}$ and $S_{ij}$ are components of the corresponding tensors. The criterion states that in a vortical structure the vorticity magnitude prevails over the strain-rate magnitude (Kolár, 2007). By using Poisson's equation for a flow with uniform density, combined with the divergence theorem for a vortex tube, Métais (2000) showed that $Q > 0$ is a necessary condition for the low pressure in a vortical structure.

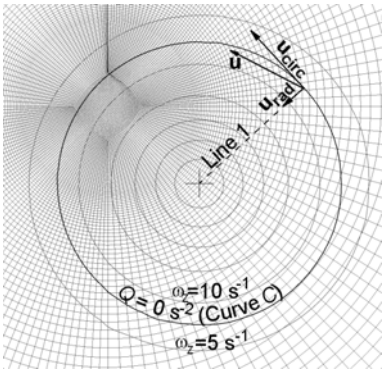


Fig. 4 Post-processing technique for determination of surface-vortex gas-core length on water surface. Black circle: curve $C$; grey circles: contour lines of vorticity in $Z$-direction, in 5 $s^{-1}$ intervals; point at center: pivot point; Line 1: line from point on curve $C$ to pivot point.

In the current study a threshold value of $Q = 0$ s$^{-2}$ was chosen as an onset for the appearance of vortical structures. The vortex radius $r_0$ on the water surface was selected as an average distance (Line 1 in Fig. 4) from the previously defined pivot point to the curve $C$. The curve $C$ was determined by the cross-section of the water's surface and the free-surface vortex structure ($Q$ = 0 s$^{-2}$). For information purposes, Fig. 4 includes the iso-surfaces of the vorticity field in the $Z$-direction ($\omega_Z$), the velocity vector $\mathbf{u}$ on curve $C$, the velocity vector in the circumferential ($\mathbf{u_{circ}}$) and the velocity vector in the radial ($\mathbf{u_{rad}}$) direction. The circulation $\Gamma$ around the pivot point was calculated from the vorticity in the $Z$-direction $\omega_Z$ as

$$\Gamma = \oint_c u_i t_i \, ds = \int_A (\varepsilon_{ijk} \frac{\partial}{\partial x_j} u_k) n_{A,i} \, dA \qquad (20)$$

where $u_i$ is a component of the velocity vector, $t_i$ is a component of a unit vector tangential to the curve $C$ and $n_{A,i}$ is a component of a unit normal vector orthogonal to the area $A$. Area $A$ is a water surface inside the curve $C$. The $\epsilon_{ijk}$ is a Levi-Civita symbol in the Einstein summation convention. The parameter $\Gamma_\infty$ was determined as the maximum value of the circulation in the range between the vortex radius $r_0$ and twice the radius.

The determination of the parameter was based on the equation specified by Sakai et al. (2008), presented with the first integral appearing in Eq. (21). Instead of computing the proposed scalar product of $\mathbf{u}$ and $\mathbf{n_C}$ (where $\mathbf{n_C}$ is a unit normal vector of curve $C$, pointing to the inner side of $C$), the following assumption was made

$$\alpha = \frac{1}{A} \oint_c u_i n_{C,i} \, ds \approx \frac{1}{A} \oint_c u_{rad} \, ds \qquad (21)$$

where $u_{rad}$ is the magnitude of the radial component of the velocity at a segment $ds$ of the curve $C$, and is pointing to the pivot point (Fig. 4). It should be mentioned that in reality the curve $C$ is a polyline (a closed polygonal chain), which means that $\mathbf{n_c}$ does not necessarily point towards the pivot point. The area $A$ represents a water surface bounded by the curve $C$.

The method for the prediction of the gas-core length was also tested with other vortex-identification methods. The $\lambda_2$ method (Jeong and Hussain, 1995) resulted in a vortex shape that was almost identical to the one obtained by the $Q$-criterion. The predicted gas-core length was close to the one predicted by the $Q$-criterion: the average relative difference between the two was approximately 1% of the values obtained by the $Q$-criterion. Other methods, such as the $\Delta$ criterion (Chong et al., 1990) and the swirling strength $\lambda_{ci}$ criterion (Zhou et al., 1999), produced a less smooth (more jagged) curve $C$.

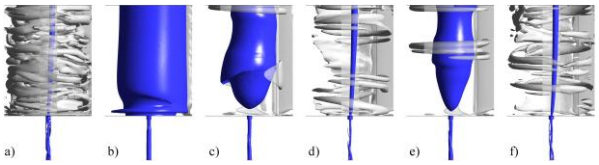


Fig. 5 Typical vortical structures (iso-surface $Q$=0 s$^{-2}$) for various turbulence models: (a) laminar (6 l/min, d$t$=0.1 s); (b) RNG $k$-ε (4.5 l/min, d$t$=0.1 s); (c) SST (4.5 l/min, d$t$=0.1 s); (d) SST-CC (6 l/min, d$t$=0.01 s); (e) SAS (6 l/min, d$t$=0.01 s); (f) SAS-CC (6 l/min, d$t$=0.01 s).

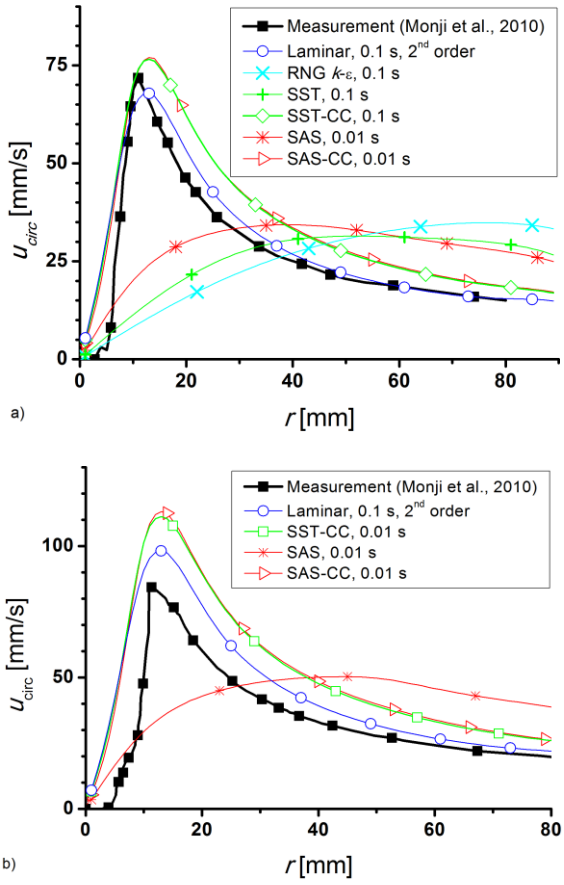


Fig. 6 Comparison of circumferential velocity around $Z$-axis with measurement data (at $Z$=0.125 m): (a) at discharge rate of 4.5 l/min; (b) at discharge rate of 6 l/min. Experimental data are from Monji et al. (2010), with permission from ASME.

## 6. RESULTS

The simulations were performed at the LSC Adria supercomputing center located at the Turboinštitut. The cluster consists of 256 IBM HS22 blade servers, each equipped with two quad-core Intel Xeon processors L5530 2.4GHz

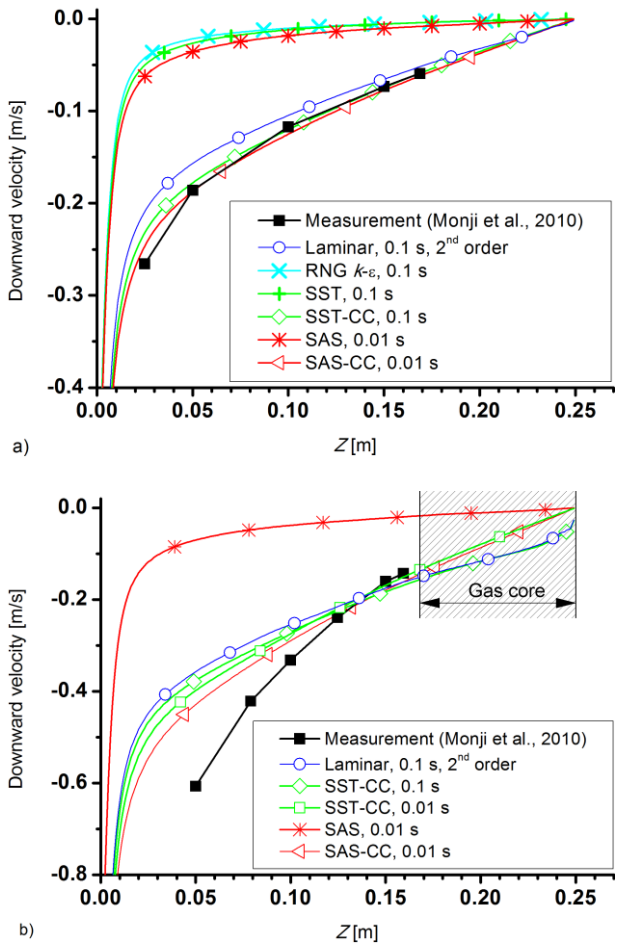


Fig. 7 Comparison of downward velocity in vortex core with measurement data: (a) at a discharge rate of 4.5 l/min; (b) at a discharge rate of 7.8 l/min. Experimental data are from Monji et al. (2010), with permission from ASME.

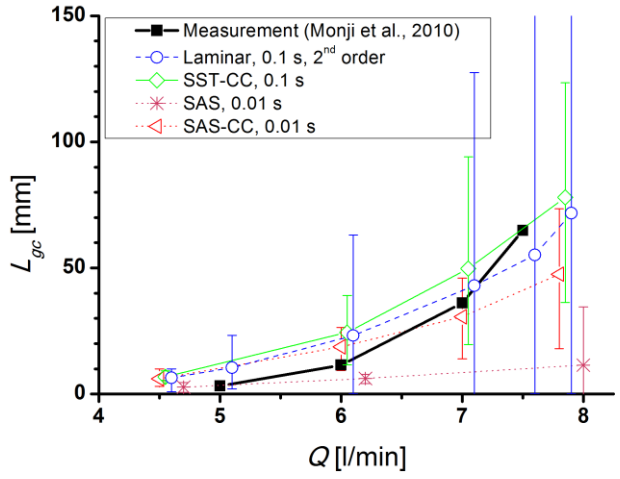


Fig. 8 Comparison of predicted gas-core length with measurement data. Some points are shifted in the abscissa direction for easier viewing (exact values can be found in Table 2). The error bars indicate the maximum and minimum calculated values. Experimental data are from Monji et al. (2010), with permission from ASME.

8MB L2 and 16 GB RAM. For fast inter-node communication an Infiniband link with the MPI protocol is used. The simulations with a small time-step size (0.001 s) demanded intensive computational resources (approximately one month on 128 computer cores), as the simulation time was large (1150 s).

### 6.1 Effect of choice of turbulence model

Fig. 5 presents some typical vortical structures resulting from the use of different turbulence models obtained by the *Q*-criterion. The $\lambda_2$ method (Jeong and Hussain, 1995) resulted in almost identical vortical structures. From the shape of the main (vertical) vortical structure it was possible to anticipate the correctness of the circumferential (Fig. 6) and downward (Fig. 7) velocity distributions. The cases with a narrow main vortical structure, such as the laminar (Fig. 5a at 6 l/min), the SST-CC (Fig. 5d at 6 l/min) and the SAS-CC simulation (Fig. 5f at 6 l/min), agreed well with the measurement data (Figs. 6 and 7). A wide vortical structure was obtained when the curvature correction was not used in the RANS simulations, such as in the RNG *k*-ε (Fig. 5b at 4.5 l/min), the SST (Fig. 5c at 4.5 l/min) and the SAS simulation (Fig. 5e at 6 l/min). In the latter three cases a large discrepancy between the measurements and the numerical results regarding the circumferential and the downward velocities could be observed (Figs. 6 and 7, respectively). The predicted downward velocity in the vortex core (Fig. 7a) was smaller than the measured one, which is an indication of vertical pressure gradients that are too small in the vortex core and which subsequently results in a vortex gas-core length that is too short (Fig. 8). On the other hand, the cases with the narrow vertical vortex structure predicted the vortex gas-core length much better, as is clear from Figs. 6 and 7. The vertical pressure gradient was larger, and therefore the predicted vortex gas-core length was longer than for the RANS models without the CC option.

The discussion in the previous paragraph indicates the role the curvature correction might have in pump-intake simulations with the RANS turbulence models. In the present article it was observed that the value of the curvature-correction function was mostly 1.25 near the boundary layer of concave walls, meaning that the modeled turbulence kinetic energy is increased there. The latter agrees well with the discussion in Patel and Sotiropoulos (1997). On the other hand, the correction function was mostly close to zero in the inner half of the vessel, near the vertical

vortical structure. This means that the modeled turbulence kinetic energy, and thus the modeled viscosity, was smaller than obtained with RANS models without the CC option. As a result of the decreased viscosity the predicted vertical vortical structure was narrow (Figs. 5d and 5f versus Figs. 5c and 5e, respectively).

From Figs. 6 and 7 it seems that the velocity predictions gradually deteriorate with the increased discharge rate (Fig. 6a vs. Fig. 6b, Fig. 7a vs. Fig. 7b), which can be associated with several reasons. In our simulations a flat-water-surface assumption was used. At higher discharge rates the (measured) length of the vortex gas-core was relatively long, e.g., at 7.5 l/min it was 65 mm, and so our estimation, based on the data extrapolation, is that at 7.8 l/min the length would be 82 mm or more (depicted as the hashed area in Fig. 7b). On the other hand, at small discharge rates only a dimple was observed in the experiment, and the numerical results show good agreement with the measurements in the velocity predictions. The second reason, applicable only to the distribution of the circumferential velocity near the vortex core, is in the experimental error due to the free-surface deformation, as mentioned by Sakai et al. (2008).

In Figs. 6 and 7 the quality of the results obtained with the laminar simulations and with the SST-CC or SAS-CC models was approximately the same. Namely, the laminar simulation predicted the circumferential velocity better than the SST-CC and SAS-CC models (Fig. 6), whereas the latter two models better predicted the downward velocity (Fig. 7a). Because of the differences in the circumferential-velocity prediction, there is also a slight difference in the calculated Reynolds number of the free-surface vortex ($Re_{vortex}$) between the laminar and the SAS-CC simulations. In Table 1, the $Re_{vortex}$ (calculated from the maximum circulation $\Gamma_\infty$ as $Re_{vortex} = \Gamma_\infty / \nu$ ) is calculated from the laminar simulations with a time-step size of 0.1 s and with the second-order scheme. The $Re_{vortex}$, obtained from the SAS-CC simulations with the time-step size of 0.001 s and with the high-resolution scheme, was slightly higher: at 4.5 l/min and at 6 l/min its values were 7,700 and 11,100, respectively.

The discrepancy of the SAS model, which predicted a too wide main vortical structure (Fig. 5e), was not expected. As shown in the studies of Davidson (2006) and Menter et al. (2010), there are cases when the unsteadiness of the flow is not sufficient and the SAS model produces either a steady-state RANS result or a low-fidelity URANS solution. This also happened in our case. Several additional tests were performed to confirm this. First, the simulations were performed with either a smaller time-step size (maximum Courant number equal to one), or a different (i.e., hybrid) advection scheme. Since the result was the same, another simulation with a hybrid advection scheme was performed on a refined mesh (4.2 million elements), using a Courant number equal to one and starting from the SAS result performed on a sparser mesh. After 12.5 s the result was approximately the same as before. On the other hand, the simulation with the Zonal LES model within the SAS model (the zone was defined inside the radius of 8 cm around the *Z*-axis inside the main vessel), using the previously described conditions, resulted in an almost inherent change of flow. After only 4 s a qualitative change of the circumferential velocity could be observed and after 12.5 s the vertical vortical structure was already narrow. Therefore, based on these results, it was concluded that the main reason for the discrepancy of the SAS model was the non-detection of the unsteadiness in the flow. It can also be concluded that the Zonal LES model may be suitable for simulations of engineering systems in which free-surface vortices appear. On the same mesh and using the same time-step size, the Zonal LES model needed approximately the same time per one time step as the SAS model.

### 6.2 Effects of time-step size and numerical scheme

The influence of the time-step size and of the numerical scheme was observed on the predictions of the circumferential velocity, the downward velocity and the length of the free-surface vortex gas core.

The time-step size or the numerical scheme selection had no impact on the results of the circumferential velocity at a discharge rate of 6 l/min (not shown), regardless of the selected turbulence model.

The choice of a numerical scheme or a variation of the time-step size (as long as it was below 0.1 s) had no significant impact on the downward-velocity prediction. The time-step size of 0.1 s resulted in a different downward-velocity distribution close to the water surface (Z=0.25 m) at high flow rates (Fig. 7b). It should be remembered that the downward-velocity gradient at the water surface is used in Eq. (18) to

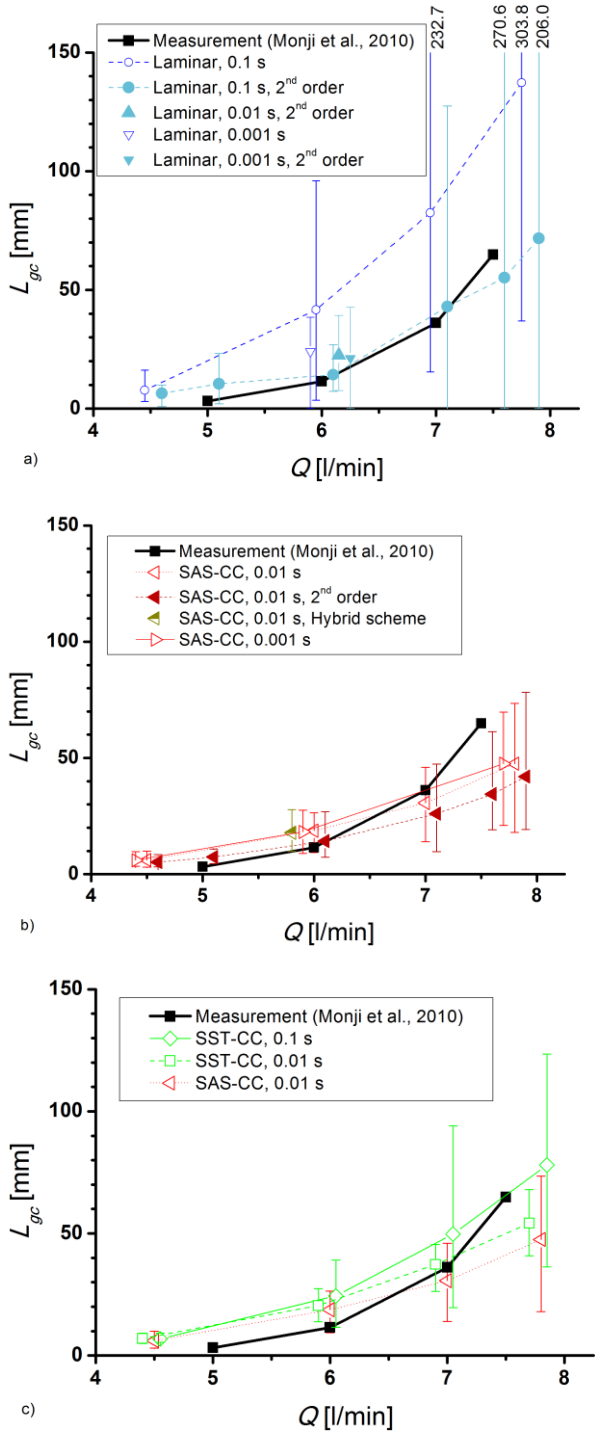


Fig. 9 Influence of time-step size and advection scheme on predicted gas-core length of free-surface vortex: (a) laminar simulation; (b) SAS-CC model; (c) SST-CC model. Some points are shifted in the abscissa direction for easier viewing (exact values can be found in Table 2). The error bars indicate the maximum and minimum calculated values. Experimental data are from Monji et al. (2010), with permission from ASME.

determine the length of the gas core of a free-surface vortex. The combination of a time-step size of 0.1 s and the HR scheme resulted in higher values of the predicted gas-core length (Figs. 9a and 9c). This was especially evident in the case of the laminar simulation (Fig. 9a). It seems that at the limiting value of the time-step size (0.1 s) the unbounded scheme produces the correct average value, whereas for the HR scheme the local values are bounded in such a way that the time-averaged value of $L_{gc}$ is increased. In order to get a proper result for the length of the gas core of free-surface vortices it is suggested to use a sufficiently small time-step size, regardless of the type of numerical scheme. The proper selection of a time-step size can be determined from the shape of the downward-velocity curve versus the depth $Z$.

In Figs. 9a and 9b it is clear that the predicted length of the free-surface gas core converges to a certain value when the time-step size is reduced. In the case of the simulations with the SAS-CC model (Fig. 9b), no difference was observed between the 0.001 s time-step size result and the 0.01 s result. In that specific case, the predicted downward and circumferential velocities obtained by the time-step sizes 0.01 s and 0.001 s are almost identical (not shown). This implies that for the SAS-CC model the use of smaller time-step sizes would not be reasonable, even though the maximum Courant number inside the vertical vortex core for the time-step size of 0.01 s was approximately ten because of the fine mesh in this area.

For small time-step sizes (0.01 s and 0.001 s) the choice of a numerical scheme did not have any major impact on the prediction of $L_{gc}$ (Figs. 9a and 9b). For such time-step sizes, it was also clear that the HR scheme always resulted in a slightly larger (absolute) downward velocity. For instance (applicable either to the laminar or the SAS-CC simulations), 5 cm above the bottom of the vessel the difference between the two schemes was up to 6 % of the measured values at a discharge rate of 4.5 l/min and up to 4.3 % at a discharge rate of 7.8 l/min.

The SAS-CC simulation predicts a shorter length of the gas core than the SST-CC simulation with the same time-step size (0.01 s) and the same advection scheme (Fig. 9c), which was the result of different predictions of the α parameter (while the circulation was nearly the same).

### 6.3 Effect of surface tension

In the simulations presented so far, the effect of surface tension was neglected. However, the

surface tension can be important for small discharge rates according to small values of the Weber number in Table 1. The correction (Ito et al., 2010) reads as $-(2\sigma c_2\sqrt{\alpha})/(\rho g\sqrt{\nu})$, where σ is a surface-tension coefficient, α is the downward-velocity gradient, ρ is the density of the water, g is the acceleration due to gravity, ν is the kinematic viscosity and $c_2$ is a function of Weber and Froude numbers of the vortex. The function $c_2$ is defined as

$$c_2 = \sqrt[3]{q/2+\sqrt{D}} + \sqrt[3]{q/2-\sqrt{D}} \qquad (22)$$

with $q = \mathrm{We}^2/32$, $D = (q/2)^2 + (s/3)^3$ and $s = \mathrm{We}^2/(16\mathrm{Fr}^2)$. For the correction, the Weber number is defined as $\mathrm{We} = \Gamma_\infty\sqrt{\rho\sqrt{\alpha}}/(2\pi\sqrt{2\sigma\sqrt{\nu}})$ and the Froude number is defined as $\mathrm{Fr} = \Gamma_\infty\alpha^{3/4}/(4\pi\nu^{3/4}\sqrt{2g})$, where $\Gamma_\infty$ is the circulation of the vortex.

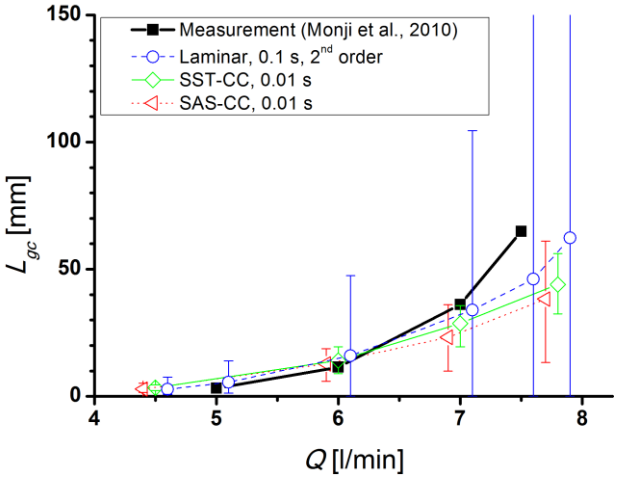


Fig. 10 Prediction of gas-core length using surface-tension correction. Some points are shifted in the abscissa direction for easier viewing (exact values can be found in Table 2). The error bars indicate the maximum and minimum calculated values. Experimental data are from Monji et al. (2010), with permission from ASME.

The correction to the prediction of $L_{gc}$ was applied to the right-hand side of Eq. (18) for some representative simulation results (Fig. 10). The amount of correction for a specific discharge rate was very similar for the laminar, SST-CC and SAS-CC simulations presented in Fig. 10. The relative amount of correction gradually decreased with the discharge rate: the average values of the correction in Fig. 10 were, for discharge rates of 4.5, 6.0, 7.0 and 7.8 l/min, equal to -53.6, -31.3, -22.8 and -17.1 % of the predicted value $L_{gc}$ defined by Eq. (18), respectively. The correction due to the surface tension resulted in considerably improved predictions of the length of the gas-core of the free-surface vortex at low discharge rates. At large discharge rates, close to the start of the bubble-detachment phenomena, the predicted length of the gas core is too low. The results for the representative laminar, SST-CC and SAS-CC simulations are similar.

## 7. CONCLUSIONS

Turbulence models were tested for their applicability in engineering systems where free-surface vortices might occur. This applicability was tested with numerical simulations of the flow in a laboratory free-surface vortex model, designed for simulations of the free-surface vortices inside a reactor vessel of the JSFR. The diameter of the cylindrical vessel (Monji et al., 2010) was 0.2 m, the diameter of the outlet pipe was 12.5 mm, and the water level was 0.25 m. The Reynolds number Re was up to approximately 13,000. The Re depended on the flow rate and was upwards limited by the start of the bubble detachment from the tip of the free-surface vortex gas-core.

At small discharge rates, the laminar, SST-CC and the SAS-CC simulations showed good agreement with the measured velocity field. In addition, the method of the vortex gas-core length seems to produce good results when a correction due to the surface tension was taken into account.

At high flow rates, close to the discharge rate when the bubble detachment from the tip of the vortex core occurs, the predicted length of the vortex gas core was too small. At high flow rates, the laminar simulation was slightly more accurate than the SST-CC and SAS-CC models.

The main reason for the discrepancies at higher flow rates is probably the neglected effect of the vortex gas core on the velocity field, because we noted a too small predicted surface gradient of the downward velocity. Additional effects can be assumptions in the method of the prediction of the gas-core length of the vortex: the assumed shape of the water-surface curvature or the assumption that the free-surface vortex could be described by the Burgers (1948) vortex model. Stepanyants and Yeoh (2008) showed that the Burgers vortex model is only valid for a small gas-core length compared to the pool height.

In our first study (Škerlavaj et al., 2010) of the laboratory free-surface vortex model, when the free-slip boundary condition was applied to all the walls, it was discovered that the SST-CC model did not predict the same circumferential velocity

as the laminar and the SAS-CC simulations. This means that for such cases the SST-CC model is not as reliable as the SAS-CC model and it might need further testing in specific environments (e.g., reactor vessels, ECCS, and pump intakes).

It should be stressed that in many engineering systems the Reynolds number is high. For instance, pump-intake model tests should normally be performed at a Reynolds number that is larger than or equal to 60,000. Because of this, the suitability of the laminar simulations in such systems is questionable. On the other hand, the SAS-CC and SST-CC models are suitable for turbulent flows. By using a SAS-CC model, we have already successfully applied the method for the prediction of the $L_{gc}$ on a case of two air-entraining free-surface vortices in a pump-intake model (Škerlavaj, 2011), which confirms the findings of this study even for a larger Reynolds number (Re=6 x $10^4$). Nevertheless, the method should be verified in other cases of free-surface vortices in order to check its limitations (or the limitations of a single-phase modeling).

The findings of this study regarding the suitability (or inappropriateness) of the turbulence models should be valid for single- and two-phase flow simulations because the shape of the free-surface vortex core in a liquid should be narrow, regardless of the type of the simulation.

## ACKNOWLEDGMENTS

We would like to express our gratitude to Professor Hideaki Monji and Dr. Kei Ito for providing answers relating to the measurement data. We would also like to express our sincere thanks to Dr. Holger Grotjans from Ansys Inc. for very fruitful conversations. Finally, special thanks are due to Rok Pavlin and Darko Ermenc for providing Fig. 1. This work was partially supported by the Slovenian Research Agency ARRS [Contract No. 1000-09-160263].

## NOMENCLATURE

| | |
|---|---|
| $A$ | Surface area |
| $C$ | Constant |
| $D$ | Diameter of vessel chamber |
| $D_{bell}$ | Diameter of bell entrance |
| $d$ | Diameter of outlet pipe |
| $F$ | Blending function |
| $F_H$ | Froude number, based on submergence $H$ |
| $F_d$ | Froude number, based on pipe diameter $d$ |
| $f_{rotation}$ | Curvature correction function |
| $g$ | Acceleration due to gravity |
| $H$ | Water level in vessel |
| $k$ | Turbulence kinetic energy |
| $L$ | Length scale of modelled turbulence |
| $L_{gc}$ | Gas core length of free-surface vortex |
| $L_{in}$ | Length of shorter side of vessel channel |
| $L_{out}$ | Length of outlet pipe |
| $L_{vK}$ | Von Karman length scale |
| $\mathbf{n}$ | Unit normal vector |
| $P_k$ | Production term |
| $Q$ | Second invariant of velocity gradient tensor |
| $Q$ | Discharge rate |
| $Q_{SAS}$ | SST SAS model's source term |
| Re | Reynolds number |
| $\mathrm{Re}_{vortex}$ | Reynolds number of vortical structure |
| $\mathrm{Re}_d$ | Reynolds number, defined with diameter $d$ |
| $\mathbf{r}$ | Position vector |
| $r$ | Radius |
| $r_0$ | Vortex radius |
| $S$ | Magnitude of strain rate |
| $S_{ij}$ | Strain rate tensor |
| $s$ | Length of curve $C$ |
| $T$ | Length of signal |
| $T_w$ | Length of window |
| $\mathbf{t}$ | Tangent vector of curve $C$ |
| $U$ | Average axial velocity at outlet surface (overbar is dropped) |
| $\mathbf{u}$ | Velocity vector |
| $u_{circ}$ | Velocity component in circumferential direction |
| $u_{rad}$ | Velocity component in radial direction |
| $V$ | Volume |
| We | Weber number |
| $\mathbf{x}$ | Position vector |
| $y$ | Wall distance |
| $y^+$ | Dimensionless wall distance |
| $Z$ | $Z$ Cartesian coordinate |
| $\alpha$ | Velocity gradient in Burgers vortex model |
| $\beta$ | Correction factor |
| $\beta$ | Constant |
| $\Gamma_\infty$ | Circulation of a vortex |
| $\Delta_{\max}$ | Maximum grid edge |
| $\delta$ | Boundary layer thickness |
| $\varepsilon$ | Turbulence dissipation rate |
| $\varepsilon$ | Statistical error |
| $\epsilon_{ijk}$ | Levi-Civita symbol |
| $\mu$ | Molecular dynamic viscosity |
| $\mu_t$ | Eddy viscosity |
| $\nu$ | Kinematic viscosity |
| $\rho$ | Density |
| $\sigma$ | Surface tension |
| $\sigma$ | Blending function |
| $\sigma_T$ | Standard deviation of signal of length $T$ |
| $\varphi$ | General scalar variable |
| $\varphi_{ip}$ | Value of variable at integration point |
| $\varphi_{up}$ | Value of variable at upwind node |

| | |
|---|---|
| $\hat{\varphi}_T$ | Mean value of signal of length $T$ |
| $\Omega$ | Magnitude of vorticity rate |
| $\mathbf{\Omega}$ | Vorticity tensor |
| $\mathbf{\Omega}^{rot}$ | Vorticity vector of reference frame |
| $\omega$ | Turbulence eddy frequency |
| $\omega_Z$ | $Z$-component of vorticity |

## REFERENCES


1. ANSI/HI (2012). *American National Standard for Rotodynamic Pumps*. Standard. Parsippany: Hydraulic Institute.
2. Ansar M, Nakato T, Constantinescu G (2002). Numerical simulations of inviscid three-dimensional flows at single- and dual-pump intakes. *Journal of Hydraulic Research* 40(4):461-470.
3. ANSYS (2011). *ANSYS CFX-Solver Theory Guide*. Canonsburg: Ansys Inc.
4. Barth TJ, Jespersen DC (1989). The design and application of upwind schemes on unstructured meshes. *Proceedings of the 27th Aerospace Science Meeting.* 9–12 January, Reno, Nevada, USA, 1-12. AIAA-89-0366.
5. Blömeling F, Pandazis P, Schaffrath A (2010). Analytical investigation of vortex formation in NPP with ANSYS CFX 12.0. *Proceedings of 7th International Conference on Multiphase Flow*. Tampa, Florida, USA, 1-10.
6. Bradshaw P (1973). *Effects of Streamline Curvature on Turbulent Flow*. Report AGARD-AG-169, Advisory Group for Aerospace Research and Development (AGARD). London: North Atlantic Treaty Organisation.
7. Burgers JM (1948). A mathematical model illustrating the theory of turbulence. *Advances in Applied Mechanics* (ed. Mises R, Karman T), New York: Academic Press, 171-199.
8. Cazalbou J-B, Chassaing P, Dufour G, Carbonneau X (2005). Two-equation modeling of turbulent rotating flows. *Physics of Fluids* 17(5):055110.
9. Chong MS, Perry AE, Cantwell BJ (1990). A general classification of three-dimensional flow fields. *Physics of Fluids A* 2(5):765-777.
10. Davidson L (2006). Evaluation of the SST-SAS model: Channel flow, asymmetric diffuser and axi-symmetric hill. *Proceedings of the ECCOMAS CFD 2006.* 5-8 September, Egmond aan Zee, The Netherlands, 1-20.
11. Durve AP, Patwardhan AW (2012). Numerical and experimental investigation of onset of gas entrainment phenomenon. *Chemical Engineering Science* 73:140-150.
12. Egorov Y, Menter F (2008). Development and application of SST-SAS turbulence model in the DESIDER project. *Advances in Hybrid RANS-LES Modelling* (ed. Peng SH, Haase W), Heidelberg: Springer, 261–270.
13. Galván S, Reggio M, Guibault F (2011). Assessment study of $k$-ε turbulence models and near-wall modeling for steady state swirling flow analysis in draft tube using Fluent. *Engineering Applications of Computational Fluid Mechanics* 5(4):459-478.
14. Hunt JCR, Wray AA, Moin P (1988). Eddies, stream, and convergence zones in turbulent flows. *Proceedings of 1988 Summer Program, Center for Turbulence Research.* Amos: NASA/ Stanford: Stanford University, 193-208.
15. Ito K, Kunugi T, Ohshima H, Kawamura T (2009). Formulations and validations of a high-precision volume-of-fluid algorithm on nonorthogonal meshes for numerical simulations of gas entrainment phenomena. *Journal of Nuclear Science and Technology* 46(4):366–373.
16. Ito K, Sakai T, Eguchi Y, Monji H, Ohshima H, Uchibori A, Xu Y (2010). Improvement of gas entrainment prediction method – Introduction of surface tension effect. *Journal of Nuclear Science and Technology* 47(9):771-778.
17. Ito K, Sakai T, Ohshima H, Tanaka N (2006). Applicability of numerical simulation to gas entrainment phenomena. *Proceedings of 5th Korea-Japan Symposium on Nuclear Thermal Hydraulics and Safety (NTHAS-5).* 26-29 November, Jeju, Korea, 384-405.
18. Jeong J, Hussain F (1995). On the identification of a vortex. *Journal of Fluid Mechanics* 285:69-94.
19. Kimura N, Ezure T, Tobita A, Kamide H (2008). Experimental study on gas entrainment at free surface in reactor vessel of a compact sodium-cooled fast reactor. *Journal of Nuclear Science and Technology* 45(10):1053-1062.
20. Kolář V (2007). Vortex identification: New requirements and limitations. *International Journal of Heat and Fluid Flow* 28(4):638-652.
21. Launder BE, Priddin CH, Sharma BI (1977). The calculation of turbulent boundary layers on spinning and curved surfaces. *Journal of Fluids Engineering* 99(1):231-239.
22. Leschziner MA, Drikakis D (2002). Turbulence modelling and turbulent-flow

computation in aeronautics. *The Aeronautical Journal* 106(1061):349-384.
23. Li HF, Chen H, Ma Z, Zhou Y (2008). Experimental and numerical investigation of free surface vortex. *Journal of Hydrodynamics* 20(4):485-491.
24. Matsui J, Kamemoto K, Okamura T (2006). CFD benchmark and an model experiment on the flow in pump sump. *Proceedings of the 23rd IAHR Symposium*. 17-21 October, Yokohama, Japan, 1-10.
25. Menter FR, Egorov Y (2010). The scale-adaptive simulation method for unsteady turbulent flow predictions. Part 1: Theory and model description. *Flow, Turbulence and Combustion* 85(1):113-138.
26. Menter FR, Gabaruk A, Smirnov P, Cokljat D, Mathey F (2010). Scale-adaptive simulation with artificial forcing. *Progress in Hybrid RANS-LES Modelling* (ed. Peng S-H, Doerffer P, Haase W), Heidelberg: Springer, 35-246.
27. Menter FR, Kuntz M, Langtry R (2003). Ten years of industrial experience with the SST turbulence model. *Turbulence, Heat and Mass Transfer 4* (ed. Hanjalić K, Nagano Y, Tummers M), New York: Begell House, 625-632.
28. Merzari E, Ninokata H, Wang S, Baglietto E (2009). Numerical simulation of free-surface vortices. *Nuclear Technology* 165(3):313-320.
29. Métais O (2000). Large-eddy simulations of turbulence. *New Trends in Turbulence* (ed. Lesieur M, Yaglom A, David F), Heidelberg:Springer, 113-186.
30. Mockett C, Knacke T, Thiele F (2010). Detection of initial transient and estimation of statistical error in time-resolved turbulent flow data. *Proceedings of the 8th International Symposium on Engineering Turbulence Modelling and Measurements*. 9-11 June, Marseille, France, 1-6.
31. Monji H, Shinozaki T, Kamide H, Sakai T (2010). Effect of experimental conditions on gas core length and downward velocity of free surface vortex in cylindrical vessel. *Journal of Engineering for Gas Turbines and Power* 132(1):012901-8.
32. Okamura T, Kamemoto K (2005). CFD simulation of flow in model pump sumps for detection of vortices. *Proceedings of the 8th Asian International Fluid Machinery Conference*. 12-15 October, Hefei, China, 625-638.
33. Patel VC, Sotiropoulos F (1997). Longitudinal curvature effects in turbulent boundary layers. *Progress in Aerospace Sciences* 33(1-2):1-70.
34. Pettersson Reif BA, Durbin PA, Ooi A (1999). Modeling rotational effects in eddy-viscosity closures. *International Journal of Heat and Fluid Flow* 20(6):563-573.
35. Rajendran VP, Constantinescu GS, Patel VC (1999). Experimental validation of numerical model of flow in pump-intake bays. *Journal of Hydraulic Engineering* 125(11):1119-1125.
36. Sakai T, Eguchi Y, Monji H, Ito K, Ohshima H (2008). Proposal of design criteria for gas entrainment from vortex dimples based on a computational fluid dynamics method. *Heat Transfer Engineering* 29(8):731-739.
37. Satpathy K, Velusamy K, Patnaik BSV, Chellapandi P (2013). Numerical simulation of liquid fall induced gas entrainment and its mitigation. *International Journal of Heat and Mass Transfer* 60:392-405.
38. Shur ML, Strelets MK, Travin AK, Spalart PR (2000). Turbulence modeling in rotation and curved channels: Assessing the Spalart–Shur correction. *AIAA Journal* 38(5):784-792.
39. Škerlavaj A (2011). *Numerical Analysis of Fluid Flow in a Pump Sump*. (in Slovene) Ph.D. thesis, University of Maribor. Available at: http://dkum.uni-mb.si/IzpisGradiva.php?id=21186.
40. Škerlavaj A, Lipej A, Ravnik J, Škerget L (2010). Turbulence model comparison for a surface vortex simulation. *IOP Conference Series: Earth and Environmental Science* 12(1):012034-9.
41. Škerlavaj A, Škerget L, Ravnik J, Lipej A (2011). Choice of a turbulence model for pump intakes. *Proceedings of the Institution of Mechanical Engineers, Part A: Journal of Power and Energy* 225(6):764-778.
42. Smirnov PE, Menter F (2009). Sensitization of the SST turbulence model to rotation and curvature by applying the Spalart-Shur correction term. *Journal of Turbomachinery* 131(4):041010-8.
43. Spalart PR, Shur M (1997). On the sensitization of turbulence models to rotation and curvature. *Aerospace Science and Technology* 1(5):297–302.
44. Stepanyants YA, Yeoh GH (2008). Stationary bathtub vortices and a critical regime of liquid discharge. *Journal of Fluid Mechanics* 604:77–98.
45. Strelets M (2001). Detached eddy simulation of massively separated flows. *Proceedings of the 39th AIAA Aerospace Sciences Meeting and Exhibit.* 8-11 January, Reno, Nevada,

USA, 1-18. AIAA 2001-0879.
46. US NRC (2006). *NRC Information Notice 2006-21: Operating Experience Regarding Entrainment of Air Into Emergency Core Cooling and Containment Spray Systems*. United States Nuclear Regulatory Commision, Washington, D.C., USA.
47. US NRC (2008). *NRC Information Notice Generic Letter 2008-01: Managing Gas Accumulation in Emergency Core Cooling, Decay Heat Removal, and Containment Spray Systems*. United States Nuclear Regulatory Commision, Washington, D.C., USA.
48. Yakhot V, Thangam S, Gatski TB, Orszag SA, Speziale CG (1992). Development of turbulence models for shear flows by a double expansion technique. *Physics of Fluids A* 4(7):1510-1520.
49. York WD, Walters DK, Leylek JH (2009). A simple and robust linear eddy-viscosity formulation for curved and rotating flows. *International Journal of Numerical Methods for Heat & Fluid Flow* 19(6):745-776.
50. Zhou J, Adrian RJ, Balachandar S, Kendall TM (1999). Mechanisms for generating coherent packets of hairpin vortices in channel flow. *Journal of Fluid Mechanics* 387:353-396.